

## Towards a physics-based understanding of fruit frost protection using wind machines

Heusinkveld, Vincent W.J.; Antoon van Hooft, J.; Schilperoort, Bart; Baas, Peter; Veldhuis, Marie claire ten; van de Wiel, Bas J.H.

**DOI**

[10.1016/j.agrformet.2019.107868](https://doi.org/10.1016/j.agrformet.2019.107868)

**Publication date**

2020

**Document Version**

Final published version

**Published in**

Agricultural and Forest Meteorology

**Citation (APA)**

Heusinkveld, V. W. J., Antoon van Hooft, J., Schilperoort, B., Baas, P., Veldhuis, M. C. T., & van de Wiel, B. J. H. (2020). Towards a physics-based understanding of fruit frost protection using wind machines. *Agricultural and Forest Meteorology*, 282-283, Article 107868. <https://doi.org/10.1016/j.agrformet.2019.107868>

**Important note**

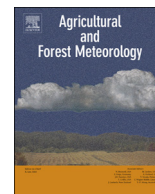
To cite this publication, please use the final published version (if applicable). Please check the document version above.

**Copyright**

Other than for strictly personal use, it is not permitted to download, forward or distribute the text or part of it, without the consent of the author(s) and/or copyright holder(s), unless the work is under an open content license such as Creative Commons.

**Takedown policy**

Please contact us and provide details if you believe this document breaches copyrights. We will remove access to the work immediately and investigate your claim.



## Towards a physics-based understanding of fruit frost protection using wind machines

Vincent W.J. Heusinkveld<sup>a</sup>, J. Antoon van Hooft<sup>b</sup>, Bart Schilperoort<sup>c</sup>, Peter Baas<sup>d,e</sup>, Marie-claire ten Veldhuis<sup>f</sup>, Bas J.H. van de Wiel<sup>\*,g</sup>

<sup>a</sup> Faculty of Civil Engineering and Geosciences, Department of Geoscience and Remote Sensing, Delft University of Technology, Delft, the Netherlands

<sup>b</sup> Faculty of Civil Engineering and Geosciences, Department of Geoscience and Remote Sensing, Delft University of Technology, Delft, the Netherlands

<sup>c</sup> Faculty of Civil Engineering and Geosciences, Department of Water Resources, Delft University of Technology, Delft, the Netherlands

<sup>d</sup> Faculty of Civil Engineering and Geosciences, Department of Geoscience and Remote Sensing, Delft University of Technology, Delft, the Netherlands

<sup>e</sup> Whiffle B.V., Delft, the Netherlands

<sup>f</sup> Faculty of Civil Engineering and Geosciences, Department of Water Resources, Delft University of Technology, Delft, the Netherlands

<sup>g</sup> Faculty of Civil Engineering and Geosciences, Department of Geoscience and Remote Sensing, Delft University of Technology, Delft, the Netherlands

### ABSTRACT

Wind machines are used in the agricultural sector to prevent or mitigate the adverse effects of night frost in spring. In this study we aim to quantify the impact of wind machine operation on the local temperature field in an orchard. To this end, a field experiment is conducted and experimental analysis is combined with numerical simulation studies in order to assess the functional relations between wind machine performance and the dominating physical processes occurring during radiative frost events.

Experimental observations showed that the temperature response strongly depends on the radial distance to the fan and the height above the surface. In agreement with previous studies, the wind machine was able to achieve rotation-averaged temperature increases of up to 50% of the inversion strength ( $\approx 3$  K) in an area of 3–5 ha at 1 m height. Furthermore, it was observed that even weak ambient winds ( $< 1$  m/s) already may cause strong upwind-downwind asymmetries in the protected area, the downwind area being larger.

The numerical model, inspired by the field experiment, showed similar spatial temperature responses as compared to observations. Interestingly, it was found that slower rotation times of the wind machine (3 to 6 min) lead to a significant increase of affected area, while the temperature enhancement itself stayed relatively constant. Variation of the horizontal tilt angle showed that, in our model, temperature enhancement was maximized between  $8^\circ$  and  $16^\circ$ . This nearly horizontal flow already facilitates efficient vertical mixing of momentum and heat, presumably due to generation of shear instabilities at the lower edge of the jet. Finally, like in the observations also the numerical result showed strong upwind-downwind asymmetry in the affected area due to background wind.

### 1. Introduction

In agricultural applications often wind machines are used to prevent or mitigate the adverse effects of night frost in spring (particularly in the fruit sector) (Scharringa, 1962; Snyder and de Melo-Abreu, 2005). Here we aim to quantify the impact of wind machine operation on the local temperature field in an orchard. To this end, a field experiment is conducted and experimental analysis is combined with numerical simulation studies in order to assess the functional relations between wind machine performance and the dominating physical processes occurring during radiative frost events. These events typically occur during clear-sky, low-wind ( $< 2.5$  m/s) nights in which, due to suppressed turbulent mixing and radiative cooling, a thermal inversion builds up from the surface (Kalma et al., 1992; van de Wiel et al., 2017). In spring, when crops are blooming and their buds are

vulnerable (Snyder and de Melo-Abreu, 2005), these events cause freezing damage with major economic losses as a result (Berz, 1992; White and Haas, 1975).

Wind machines are used to reduce these losses by eroding the thermal inversion. This can be effective, as large amounts of warm air from aloft are blown downward into the cold canopy (Bates et al., 1978; Brooks et al., 1954). The resulting local temperature enhancements near the surface will vary depending on e.g.: the strength and direction of the ambient wind, the strength of the temperature inversion of the background flow as well as on wind machine characteristics such as engine power and axial rotation time (Bey-Marshall et al., 2019). For a typical machine, 10 m in height and 130 kW of power, a temperature increase between 25% to 50% of the inversion strength ( $T_{1.5} - T_{1.5}$ ) can be achieved in areas of 3–5 ha (Evans, 1999; Snyder and de Melo-Abreu, 2005). Assessment of this performance has typically been based

\* Corresponding author.

E-mail address: [b.j.h.vandewiel@tudelft.nl](mailto:b.j.h.vandewiel@tudelft.nl) (B.J.H. van de Wiel).

<https://doi.org/10.1016/j.agrformet.2019.107868>

Received 3 July 2019; Received in revised form 18 November 2019; Accepted 5 December 2019

0168-1923/© 2019 The Authors. Published by Elsevier B.V. This is an open access article under the CC BY-NC-ND license (<http://creativecommons.org/licenses/by-nc-nd/4.0/>).

on empirical results, resulting in rather specific regression models that relate: affected area and temperature enhancement with the inversion strength (Bey-Marshall et al., 2019; Ribeiro et al., 2006). In those studies, focus was on the local temperature response depending on radial distance to the wind machine. In reality however, it is expected that the responses will also depend on the *height* at which temperature is diagnosed. Particularly in nights with radiative frost, temperature variation with height is considerable. It is therefore expected that the trees' physiological responses and fruit frost damage (quality as well as in quantity), will also depend on distance to the surface.

In this study we will therefore assess both the horizontal and vertical temperature response. Moreover, were full three-dimensional data is necessarily incomplete in field observations and conditions cannot be controlled, we will augment our analysis with Large-Eddy Simulations (LES). As such, the objective of the field experiment is to obtain a three-dimensional picture of the temperature field and to create a so-called high-quality dataset to which future simulations can be compared. Hereto, the Distributed Temperature Sensing (DTS) technique is used in combination with a point sensor grid. This provided an order of magnitude higher spatial and temporal resolution as compared to previous studies by e.g. Ribeiro et al. (2006), Bey-Marshall et al. (2019). With DTS, steep temperature gradients can be resolved over hundreds of meters (Smolen and van der Spek, 2003; Zeeman et al., 2014). It has been employed to accurately study soil heat transport (Bense et al., 2016), evaporation within canopies (Schilperoord et al., 2018), and to investigate the evolution of radiation fog (Izett et al., 2019). By applying DTS in vertical-optical arrays ('curtains') even two dimensional visualisation of turbulent structures has been made possible (Thomas et al., 2011).

The LES is used for a theoretical study on the impact of such mixing devices on both the flow field and temperature in a stably stratified environment. First, a comparison between the model outcome and the results from the field campaign is made. It will be shown that the simulations are capable of reproducing the observational findings both in a qualitative and quantitative sense. Next, the simulations are idealized and used as a tool to investigate the wind machine performance response to changing forcing parameters, like: *external* parameters: prevailing wind speed and temperature inversion strength, and *wind machine design* parameters such as: axial rotation time, horizontal tilt angle and engine power. To assess the sensitivity to these parameters, quantitative performance indicators will be put forward. This allows for the functional relations between these parameters and performance to be investigated.

The study is divided in two parts, the observational and numerical study. An overview of the field experiment is presented in Section 2. The experimental results are analysed and discussed in Section 3. The numerical study is presented in Section 4 and a similar result analysis follows in Section 5. The main results will be concluded in Section 6.

## 2. Experimental setup

### 2.1. Experimental site

The experimental part of our research was conducted between January 15, and February 4, 2019, in a pear orchard in Krabbendijke (Zeeland, the Netherlands, 51°25'44.7"N, 4°8'8.5"E). The trees are 3 m in height, were planted in rows 3 m apart which are oriented 10° West of North. The slope of the field does not exceed 1%. As the experiment was executed in winter, no leaves were present on the trees. The surface directly under the trees was covered with litter and composting leaves, whereas in between the tree rows matured grass was present (shown in Appendix A.2). In Fig. 1, an aerial image of the site is shown. It can be seen that the orchard is separated by a dike from the Oosterschelde, a large estuarine water body.



Fig. 1. Aerial image of the experimental site. The Oosterschelde is visible on the right side of the image. Markings are explained in the legend of Fig. 3. Image adapted from Google Maps.



Fig. 2. The wind machine in the pear orchard, with the engine mounted at the bottom of the tower. In the back, the dike is visible.

### 2.2. Wind machine specifications

The wind machine was installed in 1991 and was manufactured by Orchard-Rite® (Fig. 2). It has a 10.5 m hub height and 5 m diameter double-bladed fan which blows air 7° downward. The wind machine was powered by a propane engine with a design power of 134 kW. The wind machine blades rotated at 540 rpm and the fan hub revolved around the tower once every 5 min.

### 2.3. Measurement setup

The objective of our setup was to obtain a three-dimensional impression of the temperature field around the wind machine. Hereto, we combined horizontal grids of point observations (at two vertical levels), with Distributed Temperature Sensing (DTS) providing both detailed vertical profiles and horizontal line observations. Wind measurements were taken during fan operation to assess the wind speed as a function of distance from the wind machine. Additionally, on-site weather stations were installed in order to capture the local meteorology. This setup is shown in Fig. 3.

Distributed Temperature Sensing (DTS) is a technique to measure the temperature along a fiber optic cable with high spatial (0.3 m) and temporal resolution. This is done using the temperature dependent backscatter signal of a laser pulse (Selker et al., 2006; Smolen and van der Spek, 2003). Two different cables were used, a thick 6 mm PVC reinforced duplex fiber optic cable (response time of  $\approx 5$  min) and a thin 1.6 mm fiber optic cable ( $\approx 30$  s). Both were measured using a Ultima-S™ system. The thick cable was deployed in a double-ended configuration by looping back through the second core. Both, forward and backward measurement were averaged over 5 s. The thin cable was

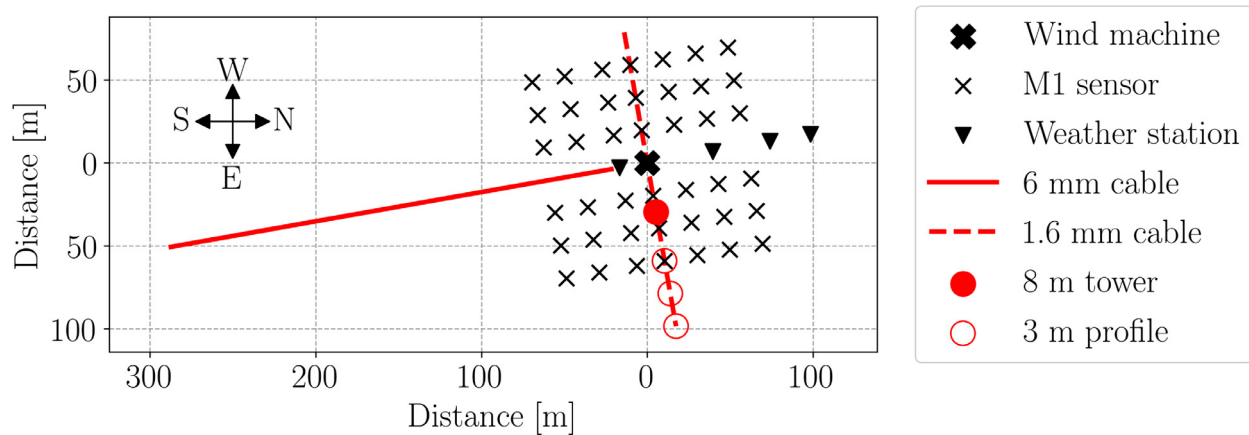


**Fig. 3.** Schematic of the setup with relative distance to the wind machine. The red elements are constructed using DTS. The 6 mm cable is attached to the trees at 1 m above the surface, and the 1.6 mm cable at 1m as well as 0 m (surface measurements). (For interpretation of the references to colour in this figure legend, the reader is referred to the web version of this article.)

used in a single-ended configuration, with an averaging period of 10 s. For calibration, the cables went twice through a well-mixed water bath which was monitored by a Pt100 temperature probe. The calibration was done using the internal reference of the Ultima, and the bath, in combination with the python DTS calibration package by [des Tombe and Schilperoord \(2019\)](#). For the single-ended configuration this setup may result in a bias; however this appeared insignificant for our results. Using this setup  $\approx 0.1$  K of temperature accuracy is achieved.

The configuration of the cables is shown in [Fig. 3](#). The thick cable of near 300 m length was oriented North-South and placed at  $\approx 1$  m above the surface as to represent in-canopy conditions. The thin cable ran 100 m East and 80 m West of the wind machine at a height of  $\approx 1$  m and 0 m along the surface for the surface temperature response. Additionally, the thin cable was used to measure four vertical temperature profiles. An 8 m profile (suspended freely) using a pneumatic tower and three 3 m profiles that were supported every 1 m by a metal framework. The DTS was operated during one particular Intensive Observational Night (January 20th/21st), in which conditions were predominantly clear skies and weak winds, such that a strong inversion could develop (see below).

For the horizontal grids, 84 tempmate.<sup>®</sup> M1 temperature loggers (logging interval 1 min) with an external temperature sensor were used. The sensors have a resolution of 0.1 K, an accuracy of 0.5 K and a response time of 30 s. Using the sensors, a 120 m by 120 m grid was constructed at 1 m and 2 m heights as shown in [Fig. 3](#).

Due to practical limitations both the M1 loggers and the DTS cables are unshielded and thus do not directly measure the air temperature. During the night time conditions the sensor temperature is expected to be lower than the air temperature, due to the radiative loss to the open sky. As our results focus on relative temperature differences, conclusions are not expected to be influenced significantly.

Wind measurements were done using two types of devices. Four Peakmeter<sup>®</sup> MS6252B propeller anemometers (accuracy  $\pm 2\%$ , sampling frequency 2.5 Hz) and two Testo, Inc. 405i hot-wire anemometers ( $\pm (0.1 \text{ m/s} + 5\%)$ , 0.5 Hz). The six devices were mounted on top of a 3 m height handheld tripod. Because of the superior sampling frequency, the propeller anemometers were used to measure the wind speed induced by the fan, while the hot-wire anemometers were used to measure the background wind.

Four Davis<sup>®</sup> Vantage Pro2 weather stations were installed to provide additional weather information and logged with an interval of 10 min.

### 3. Experimental results

#### 3.1. Local weather conditions

During the experimental period, one radiative frost night occurred on January 20. As a winter case is considered, temperatures were low in general over the full diurnal cycle. The temperature as measured by the weather station of Woensdrecht (10 km East of Krabbendijke), is shown in [Fig. 4](#). This station is used, since it was undisturbed by wind machine operation and is capable of reporting cloud cover (shaded). It can be seen that surface temperature responded strongly ( $\approx 2$  K) to the passing of semi-transparent altocumulus clouds. Apart from this period, the night was predominantly clear sky. The 10 m wind from the East, ceased to values below 1 m/s. During the experiment the relative humidity was  $\approx 90\%$ . The Oosterschelde had low-tide, which favours the occurrence of stable conditions (see [Appendix A.1](#)).

Where temperature observations at Woensdrecht represent two levels only, a more detailed vertical profile was obtained on-site, as to characterize the nocturnal inversion strength. The average profile around 00:00 is shown in [Fig. 5](#) (black line). The ‘off’ and ‘on’ periods refer to ventilator operation and will be elaborated on later. An S-shaped inversion is visible, with strong gradients appearing near the surface and the canopy height (3 m). The,  $T_{15} - T_{1.5}$ , inversion strength, as often reported in literature, was in the order of 3 K, i.e. a moderately strong inversion ([Evans, 1999](#)).

In the figure, hub height temperature (at 10.5 m) is estimated from the linear extrapolated ‘off’ profile and plotted as a vertical black line. In case of ‘optimal’ mixing, the temperature at the surface would tend

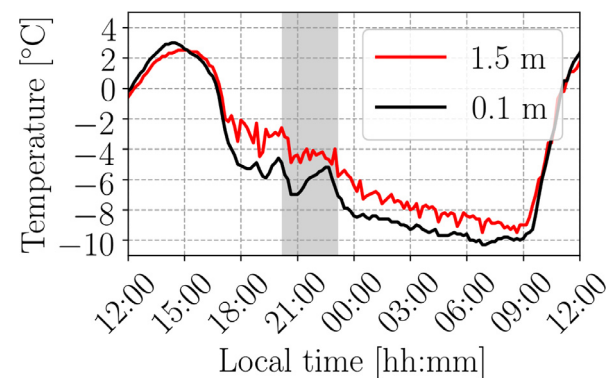


**Fig. 4.** Temperature at Woensdrecht starting noon January 20. The shaded area indicates the passing of semi-transparent altocumulus clouds. Local time was UTC+1.

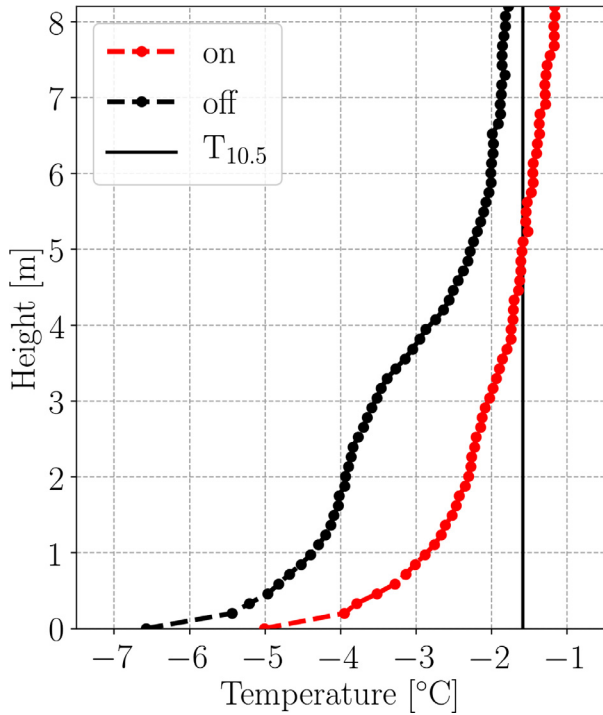


Fig. 5. Averaged vertical temperature profiles using DTS for fan on and off periods. The 10.5 m temperature is based on a linear extrapolation of the ‘off’ profile. Note that the (unshielded) sensor temperature is displayed (see text).

towards this temperature. Hence, the maximum temperature increase is defined as:

$$\Delta T_{\max}(h) = T_{10.5} - T(h) \quad (1)$$

in which  $T(h)$  is the undisturbed, ‘fan off’, temperature at a certain height,  $h$ . Expression (1) will be used to normalize results to allow for a comparison between heights.

### 3.2. Wind machine operation and generated airflow characterisation

Wind machine operation started at 21:48 and stopped at 23:42 (UTC+1), using 100 L of propane gas. From before the start of operation till 23:06, semi-transparent altocumulus clouds were present on-site. The analysis will focus on the clear sky period from 23:06 onwards, assuming minimal effect of the preceding cloud period.

When in operation, the wind machine accelerates air and generates a turbulent *jet*. When seen from above, the jet sweeps a certain area over 360 degrees due to the rotation of the hub on the fan tower. At 3m height the air speed maximum was diagnosed as a function of distance to the fan (Fig. 6). The measurement period spanned one hour during which the 3 m mean wind ( $0.5 \pm 0.3$  m/s) came from the East-Northeast ( $67 \pm 4^\circ$ ). A strong,  $\approx 2$  m/s, upwind-downwind (East-West) asymmetry is visible. Interestingly, due to the fan elevation at 10 m (blowing down at  $7^\circ$ ), the closest observation at the East side appears to be out of the jets’ reach (fan blowing ‘over’ the sensor).

### 3.3. Horizontal temperature response and influence distance

The temperature measurements done using the horizontal DTS cables are shown in Fig. 7 in which time is expressed relative to the starting time of the wind machine. As in the Woensdrecht data, when the clouds disappeared, a clear drop in temperature was measured. In addition, the 5 min rotation period of the wind machine can be identified. Note that the data in Fig. 7a is ‘smeared’ out as compared to the others due to the slower response time of the cable (5 min vs 30 s). The light ‘yellow bar’ in Fig. 7b and c represents a strong temperature signal

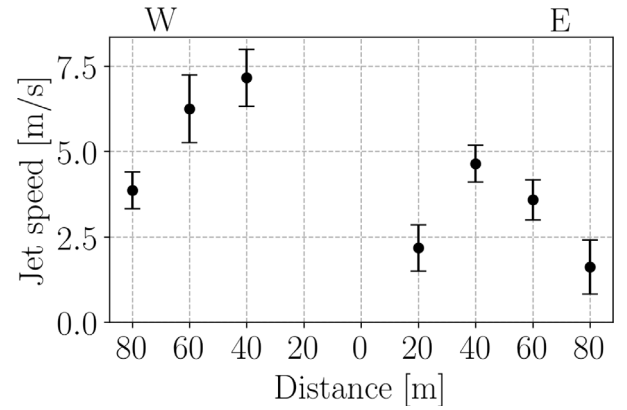


Fig. 6. Jet speed based on four vane anemometer measurements at a height of 3 m. W-E refers to the West and East-side of the ventilator (with mean wind from the East).

due to heat and radiation released/emitted by the engine reaching  $O(15)^\circ\text{C}$  and  $O(40)^\circ\text{C}$ , respectively. Although the majority of this heat may ‘leave’ the system through vertical convection, it does have the potential to raise the temperature in addition to the ventilator. The average energy consumed by the engine was  $\approx 370$  kW, generating  $\approx 240$  kW in exhaust heat. This is equivalent to an air volume of  $\approx 10^5$  m<sup>3</sup> being raised by 1 K over one rotational period, 300 s.

If the weather would have been truly stationary, the average temperature change caused by the wind machine could have been assessed by simply subtracting the temperature before fan operation (‘reference state’, fan off) from the temperature after a few rotations (fan on). However, our conditions of interest, i.e. clear skies, only appeared during and after fan operation. We will therefore refer our results during operation (88 - 108 min) relative to the (cold) reference state after the operation (119–134 min). The results are shown in Fig. 8.

For the South cable, Fig. 8a, a spatial North-South slope in the temperature is visible during the fan off period. We hypothesize that this is due to a ‘thermal memory’ of the physico-biological system (also present in Fig. 8b and c). The data of Fig. 8b is gathered perpendicular to the data in Fig. 8a and aligns with the mean wind direction. As with the jet speed (Fig. 6), an upwind-downwind asymmetry is present in 8 b.

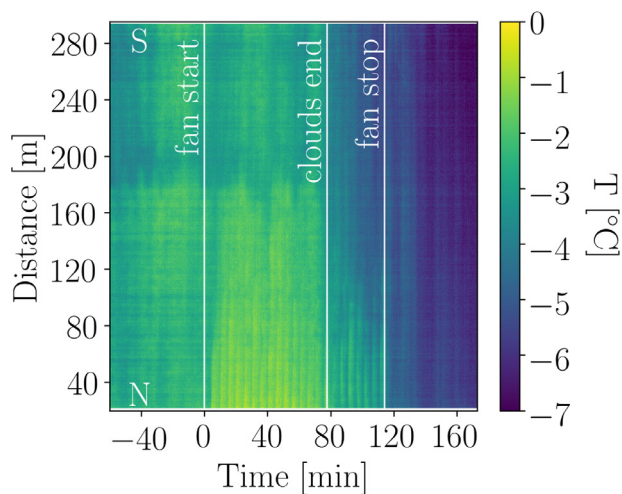
Interesting, sharp temperature ‘spikes’ appear in Fig. 8b and c. Those are no artifacts, as they are caused by actual differences in surface cover: the signal had a spatial periodicity of 3 m, which coincides with the row spacing (surface cover shown in Fig. 26 of Appendix A.2).

To determine to the average temperature change from Fig. 8, the black line cannot simply be subtracted from the red line, due to the overall temperature trend that occurred during the night (compare also Fig. 4). This can be corrected for by using a height dependent reference temperature which was not influenced by the wind machine. This reference was chosen based on wind direction and the temporal responses seen in Fig. 7. For the 1 m height measurements, the averaged South section temperature from 270 m to 280 m was taken as a reference (Fig. 8a). For the 0 m height measurements, the averaged East section temperature from 91 m to 100 m was taken (Fig. 8c).

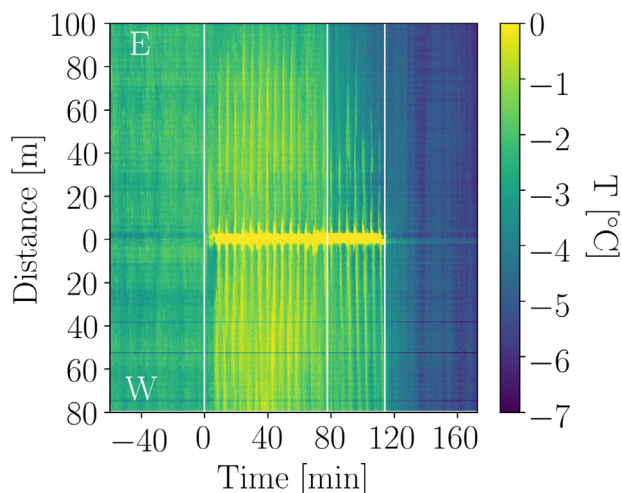
Using the South cable from Fig. 8a as an example: The 270 m to 280 m temperature is averaged, after which both the red and black curve are offset by this reference temperature. They are then subtracted from each other to get the temperature change due to fan operation at every location along the cable. This temperature difference can formally be expressed as:

$$\Delta T(\vec{r}) = \sum_{t \in \text{on}} (T(\vec{r}, t) - T_{\text{ref}}(h, t)) - \sum_{t \in \text{off}} (T(\vec{r}, t) - T_{\text{ref}}(h, t)) \quad (2)$$

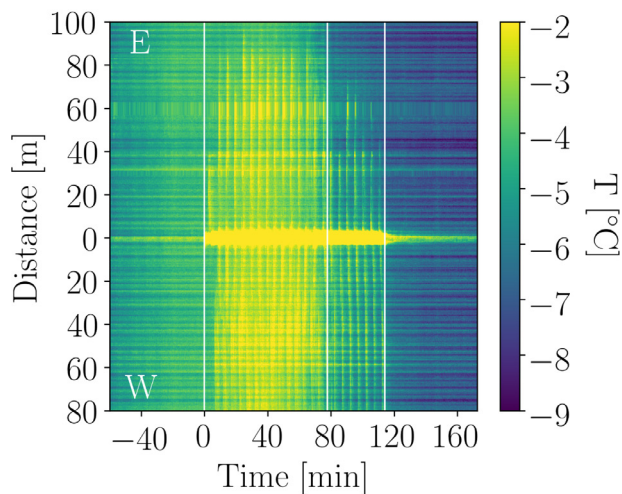
in which  $h$  is the height of the location vector  $\vec{r}$ , time  $t$  is in the fan ‘on’



(a) South cable at 1 m height.

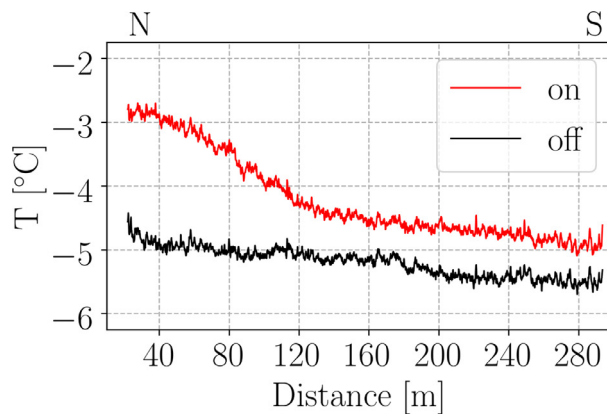


(b) West-East cable at 1 m height.

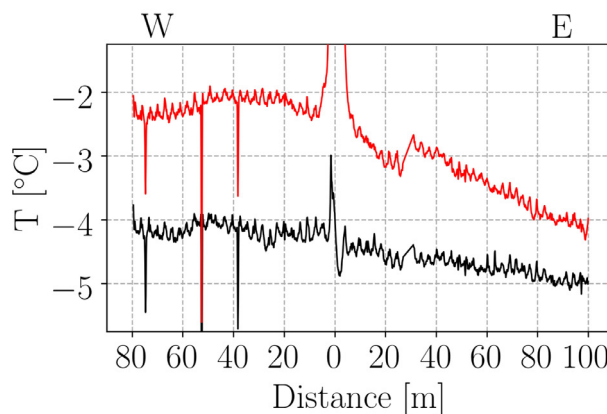


(c) West-East cable at 0 m height.

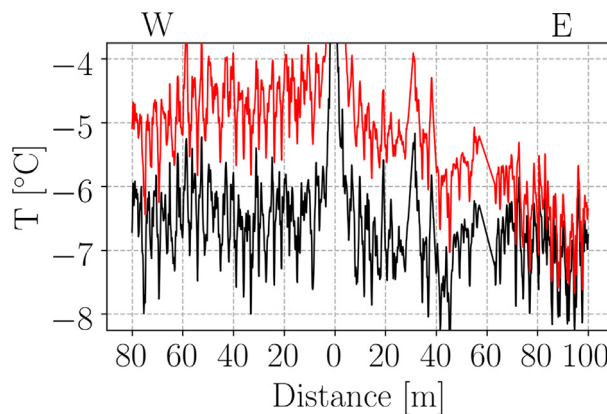
**Fig. 7.** Time series of the horizontal DTS measurements. Events are indicated by the white lines. Clouds were present before the start of this time series. NWSE denote the orientation of the cables. Note that the (unshielded) sensor temperature is displayed, as in Figs. 8 and 12 (see text).



(a) 1 m height South cable.



(b) 1 m height West-East cable.

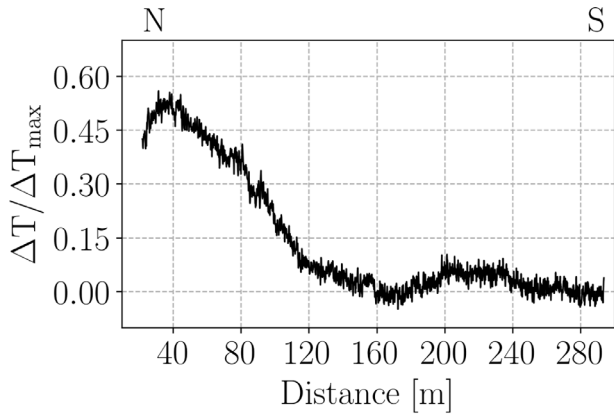


(c) 0 m height West-East cable.

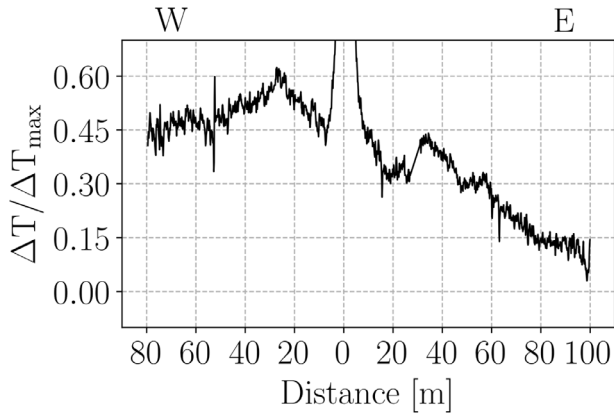
**Fig. 8.** Horizontal DTS measurements averaged over the fan on and fan off periods. NWSE denote the orientation.

or 'off' period,  $T$  is the measured temperature and  $T_{ref}$  is the reference temperature as explained before. This procedure is carried out for all three horizontal DTS sections. Afterwards, these temperature changes are normalized by  $\Delta T_{max}(h)$  as defined in Eq. (1) and the results are shown in Fig. 9. The ratio of  $\Delta T$  over  $\Delta T_{max}$  will be referred to as the efficiency.

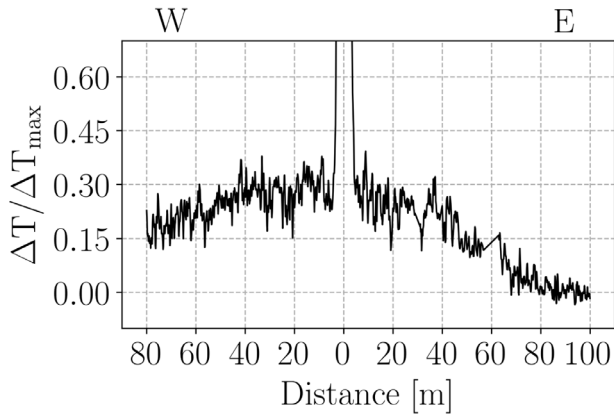
To assess the distance at which the wind machine had an effect, the *distance of influence*, a criterion needs to be defined. In literature often the distance at which a certain temperature fraction of the inversion strength is reached is used (Bey-Marshall et al., 2019; Ribeiro et al., 2006). Here however, a Gaussian model is introduced which fitted well



(a) 1 m height South cable,  $\Delta T_{\max} = 2.75$  K.



(b) 1 m height West-East cable,  $\Delta T_{\max} = 2.75$  K.



(c) 0 m height West-East cable,  $\Delta T_{\max} = 4.99$  K.

Fig. 9. Efficiencies for the horizontal DTS sections. NWSE denote the orientation.

to the efficiency data in Fig. 9. This method works as follows; a priori a Gaussian curve, Eq. (3), is assumed for the temperature influence as a function of distance at a certain height.

$$f(r) = a \exp\left(-\frac{(r - b)^2}{2c^2}\right) + d \quad (3)$$

This function is least square error fitted to the efficiency curves by varying a, b, c, and d. This is illustrated by Fig. 10. We define the distance of influence as b+c and the fitted maximum efficiency as a+d.

This model is applied to all the horizontal DTS measurements

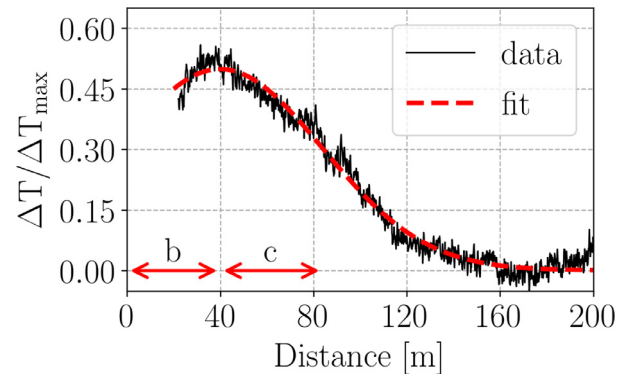


Fig. 10. Illustration of the Gaussian model. Fit to Fig. 9a. Arrows indicate the fitted values for the parameters b and c.

Table 1

Distance of influence and maximum efficiency based on the Gaussian fit. Least square error fit uncertainties are reported when greater than the least significant digit.

Section	Distance [m]	Max Efficiency
South 1 m	$83.9 \pm 0.3$	0.50
West 1 m	$104.7 \pm 76.3$	0.53
East 1 m	$67.8 \pm 1.3$	0.37
West 0 m	$76.6 \pm 29.5$	$0.53 \pm 0.01$
East 0 m	$51.5 \pm 0.6$	$0.44 \pm 0.01$

resulting in the fitting parameters shown in Table 1.

In general, the Gaussian model fitted well and captured the observed asymmetries between East and West. Note that the fitting error became large when the efficiency did not yet approach zero. Based on these influence distances and Fig. 9 the area in which a temperature enhancement was achieved is crudely approximated to be 3–5 ha at 1 m height.

### 3.4. Mixing efficiency profiles and temporal responses

The 8 m averaged vertical profile was shown in Fig. 5. To get the efficiency for all four vertical temperature profiles, the same procedure as in the previous section is used. The background temperature was corrected for by using the 1 m height reference (average over South section from 270 m to 280 m), which was taken to be representative for the whole canopy. These results are shown in Fig. 11.

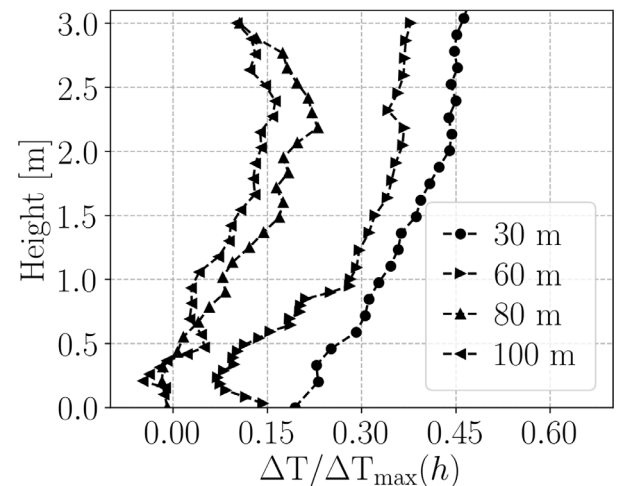


Fig. 11. Efficiency of mixing within the canopy for various distances eastward/upwind of the fan. Note that  $\Delta T_{\max}$  is height dependent.

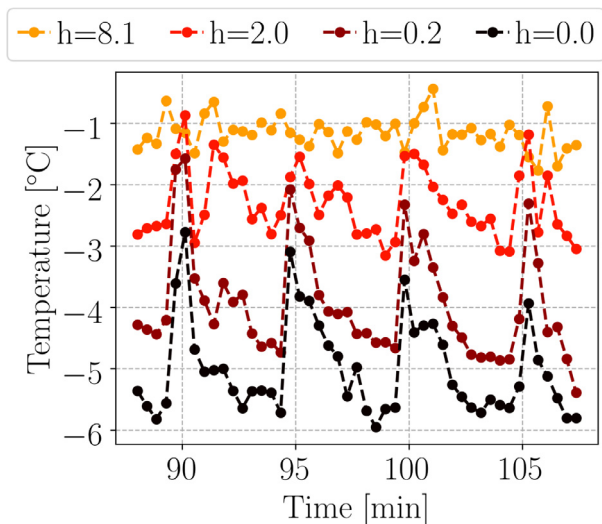


Fig. 12. Temperature response at different tower heights, 30 m East from the wind machine.

There is an interesting dependence on distance: the further away from the fan the more the temperature enhancement is confined to the canopy top. Close to the fan, the flow over the canopy is strongest as is the contrast with the weak in-canopy flow. Presumably, vertical mixing is generated by shear instabilities (Kelvin Helmholtz type) as often encountered in flows over canopies (Boing et al., 2010; Finnigan et al., 2009). As those effects are strongest near the fan, there mixing will penetrate more effectively. Note that the cold biomass and strong inversion near the surface could play a role in damping this penetration. To study this behaviour further, temporal responses at different heights are shown in Fig. 12.

The 5 min fan revolution cycle causes  $\approx 3$  K of temperature variation at 0 m and 0.2 m height, damping to  $\approx 2$  K at 2 m and less than 1 K at 8 m. This amplitude difference is in part explained by  $\Delta T_{\max}(h)$  decreasing with increasing height,  $h$ . Note that after each temperature ramp, cooling of the air towards its reference state is faster near the surface which could be a result of the cold biomass present. Interestingly, the 0 m measurement laying on grass and 0.2 m measurement just above, had a similar amplitude and decay. Hence at this location, no extra ‘damping’ of the temperature signal due to direct contact with the grass was measured.

### 3.5. Efficiency contours

Using the sensor grid, the goal was to get two-dimensional plane measurements at two heights. Due to water/frost damage, the grid data at 2 m height was lost. For the 1 m data a similar procedure as before was used to get the efficiency. The contour plot is shown in Fig. 13.

The influence of wind direction on affected area is clearly visible. Also, the affected area is larger than the size of the grid network, which agrees with the previous analysis of the DTS showing that this area is 3–5 ha. Finally, note that the impact of engine heat appears to be visible as well, as the efficiency exceeds 1 near the fan.

## 4. Simulation methods

In order to further study the dynamics of wind machine operating in a stable stratification, Large-Eddy Simulations are performed. This approach facilitates to study the local dynamical response to changing forcing parameters. We focus on the effects of *external* parameters such as: the prevailing wind speed ( $U$ ) and the strength of the temperature inversion ( $N$ ), and the parameters that govern the *wind machine design*: the rotation time ( $\tau$ ), the engine’s power output ( $P$ ) and rotor tilt

angle ( $\alpha$ ). (see Fig. 14).

### 4.1. The numerical solver and modelled physics

The LES is based on the partial differential equation solver Basilisk which is available at [www.basilisk.fr](http://www.basilisk.fr) (Popinet, 2015). For details on the model we refer to van Hooft et al. (2018a). The numerical model solves the filtered Navier-Stokes equations under the Boussinesq approximation (Wyngaard, 2010). The solver is second order accurate in space and time and uses a fractional-step method (Castillo-Castellanos, 2017; Popinet, 2009). The advection term is computed using the Bell-Collella-Glaz scheme (Bell et al., 1989) and the pressure is calculated using a multi-grid strategy (Brandt, 1977). The turbulent mixing of heat and momentum at the sub-grid scale is parametrized with the eddy-viscosity closure formulated by Vreman (2004).

Due to the strongly localized dynamics around the wind machine, an adaptive octree based grid is used (see van Hooft et al. (2018a)). In this work, grid adaptation is based on an estimated discretization error in the solution fields for the wind components and temperature. The error thresholds or so-called ‘refinement criteria’, are set to 0.5 m/s and 0.35 K, respectively, balancing numerical accuracy and computational effort (see van Hooft et al. (2018b)).

Besides the Navier-Stokes equations and eddy-viscosity closure, the modelled physics consist of: a soil scheme, a wind forcing, a wind machine momentum source and a source representing engine heat. The soil scheme is based on simple land-atmosphere coupling similar to van de Wiel et al. (2017) and is implemented as in van Hooft et al. (2019). The wind forcing is implemented near the horizontal boundaries (10% of the domain size) as a slow relaxation towards a profile. In this volume the temperature is also forced, to simulate the advection of ‘fresh’ air. The wind machine momentum source is based on a power formulation (Appendix B.1) in which power can be interpreted as the work done on the air per unit time. It is assumed that the process generating this power has an efficiency of 10%, such that the remaining 90% is released as engine heat.

Note this model is a crude simplification of complex reality and therefore necessarily incomplete. Specially, we have omitted to implement the geometry of tree rows, have assumed horizontal homogeneity and no background turbulence is present (VSBL). Here we aim for simplicity to study qualitative behavior due to ventilator operation. Things such as the realistic implementation of tree geometry is beyond the scope of the present study (e.g. Finnigan et al. (2009)).

### 4.2. Simulation setup

Two cases are defined. The setup of the first case is inspired by the experimental setting in order to enable a comparison between model results and observations. The second case uses idealized settings and is used for sensitivity studies.

In both a  $700^3 \text{ m}^3$  domain is chosen with periodic boundary conditions in the horizontal dimensions. The bottom and top boundary conditions are set to no-slip and stress-free, respectively. The maximum resolution is set to  $512^3$  corresponding to a minimum grid size of  $\approx 1.37$  m. The wind machine momentum forcing is turned on after 30 s and the simulation runs for four fan rotation periods.

For the Krabbendijke case, the wind machine hub height is set to 10.5 m, rotor diameter to 5 m, rotation time,  $\tau$ , to 300 s and tilt angle,  $\alpha$ , to  $7^\circ$ . The power of the wind machine,  $P$ , is set to  $\approx 14$  kW which gave the closest agreement between the jet velocity of the simulation and the observation. The initial wind profile,  $U$ , is prescribed to be logarithmic, according to Eq. (4) with  $h_0 = 0.1$  m. The magnitude is set by the choice of prefactor  $U_f$ . Here,  $U_f = 0.1$  m/s such that the wind speed at the hub height is  $\approx 0.5$  m/s.

$$U(h) = U_f \ln\left(\frac{h + h_0}{h_0}\right) \quad (4)$$

The initial temperature profile is also assumed to be logarithmic, according to Eq. (5). As such, S-shape effects like in Fig. 5 are omitted for simplicity. Here we choose  $h_1 = 0.2$  m and  $T_f = 1$  K which gave the closest fit to observations. The surface temperature is set at 0°C.

$$T(h) = T_f \ln\left(\frac{h + h_1}{h_1}\right) \quad (5)$$

After initialization, the temperature and wind profiles are relaxed at the boundaries as described in the previous section. The soil-heat coupling strength,  $\lambda$ , is chosen as  $5 \text{ Jm}^{-2}\text{s}^{-1}\text{K}^{-1}$  which represents the coupling of a grass surface (van de Wiel et al., 2017).

For the sensitivity study a different case is defined as a standard, from which individual parameters are varied. The same domain, resolution, boundary conditions, surface coupling, soil temperature and wind machine settings are set as in the Krabbendijke case. However, from the wind machine parameters, the rotation period is shortened to 240 s and the engine heat is turned off. Default, the inflow is set to zero. Next, wind speed effects are analysed by varying  $U_f$  (Eq. (4)). For temperature, a simple linear profile with a slope of  $N^2 = 0.3 \text{ K/m}$  is set:

$$T(h) = N^2 h \quad (6)$$

During simulations, diagnostics are performed similar to the DTS and wind measurements done during the field experiment. We diagnose with 1 m and 1 s resolution at the those locations for which also observations were available. In addition, four temperature slices at 0.5, 1, 2, and 4 m height are outputted with a 2 m spatial and 5 s temporal resolution.

The descriptive overview of the setup herein can not do justice to all the exact details of the implementations. As such, the used methods are documented and are made freely available via the Basilisk website: [www.basilisk.fr/sandbox/vheusinkveld](http://www.basilisk.fr/sandbox/vheusinkveld), Krabbendijke case: /krabbendijke.h, idealized case: /idealized.h.

## 5. Simulation results

### 5.1. Comparison with observation

The maximum speed of the passing jet was averaged over the four rotations and is shown in Fig. 15. The 2 m/s asymmetry in maximum jet speed between West and East as seen in the experimental data was not present. However, a similar upwind-downwind asymmetry is seen in the decay of the jet speed with distance.

For comparing the DTS temperature measurements, the experimental ‘clear sky, fan on’ data was used. This data was shifted in time such that a passing of the jet occurred synchronous with the simulation data. The results are shown Fig. 16 for which the experimental data was offset by 5.5 K. In general, there is a remarkable qualitative agreement between simulation and experiment considering the limited physics that was implemented. This suggests that the most dominant processes are represented by the simulations. Besides this, the simulation data shows more detail due to the instantaneous response time and higher sampling as compared to the field experiment.

The vertical time series, Fig. 16a, shows the temperature responses near the surface lasting longer in the simulations with transitions being sharper. Horizontally from West to East, Fig. 16b, upwind (East) temperature responses were similar between experiment and simulation at equal distances while downwind (West) responses showed a discrepancy. The latter might be a consequence of the differences in jet speed (Fig. 15). The horizontal North-South time series, Fig. 16c, also shows similar temperature responses at equal distances. Note that the response to the first rotation is distinctly different from the others. This is caused by the simulation start-up, with temperature and wind fields being disturbed for the first time. For this reason, the analysis will focus on the three rotations thereafter.

From the numerical data, a horizontal slice at 1 m is taken to

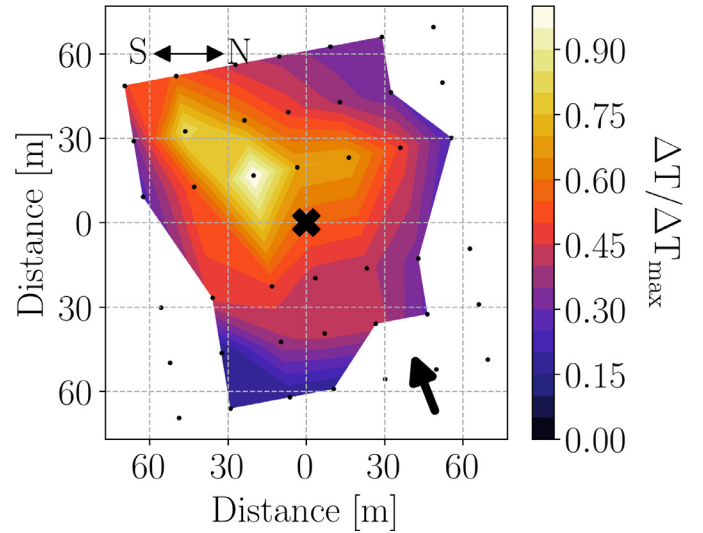


Fig. 13. Efficiency contours near the wind machine at 1 m height using the M1 loggers (dots). At missing data points water/frost damage occurred. The wind direction is denoted by the arrow.

determine the efficiency in this plane. The procedure differs slightly as compared to the experiment since the temperature field is initialized and thus known. In general the procedure is as follows:

1. The temperature field is averaged over the last three rotations and the initialized temperature field is subtracted.
2. A slice is chosen at a particular height,  $h$ , and is normalized by  $\Delta T_{\max}$ . Eq. (1), using the temperature profile as defined in Eq. (5) or (6).

The result is shown in Fig. 17 (slice at 1m height). Simulated efficiencies reached similar values as in the experiment. The effect of wind direction is distinctly visible. However, based on the comparisons made in Figs. 15 and 16 b this wind dependence may be slightly overestimated.

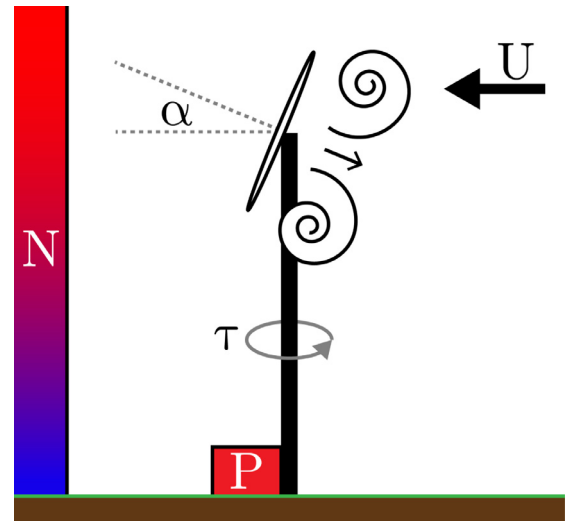


Fig. 14. Schematic of the simplified model involving the wind machine. External parameters: the prevailing wind speed ( $U$ ) and the strength of the temperature inversion ( $N$ ). Wind machine design parameters: the rotation time ( $\tau$ ), the engine’s power output ( $P$ ) and rotor tilt angle ( $\alpha$ ).

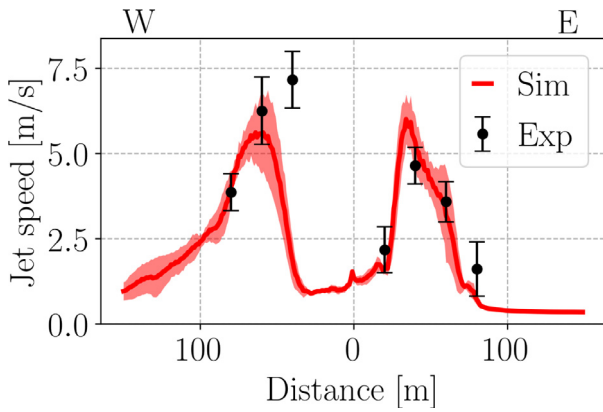


Fig. 15. Jet speed comparison between the simulation and experiment. The shaded area represents the standard deviation over four rotational averages of the maximum jet speed.

5.2. Sensitivity to forcing parameters

The comparison in the previous section shows that the model is able to mimic the response of the temperature field due to fan operation. In this section, we aim to quantitatively compare changes in this temperature response as a result of varying parameters. For this, a performance measure needs to be defined. The full three-dimensional temperature field could be investigated. However, this data is high in dimensionality and does not directly reflect things that are of practical importance, namely:

- What is the area influenced by the wind machine at different heights?
- What is the achieved average temperature increase or efficiency in this area?

Hence performance measures will be defined as:

1. A two-dimensional efficiency slice is made as described in the previous section. An example of this is shown in Fig. 18.
2. For every angle in the plane (discretized,  $\Delta\beta = 3.75^\circ$ ), the distance of influence is estimated using a Gaussian fit (similar to the example in Fig. 10) denoted by the white dashed line in Fig. 18.
3. The area enclosed by this line is defined as the influenced area. The efficiency in this area is averaged to get the other measure.

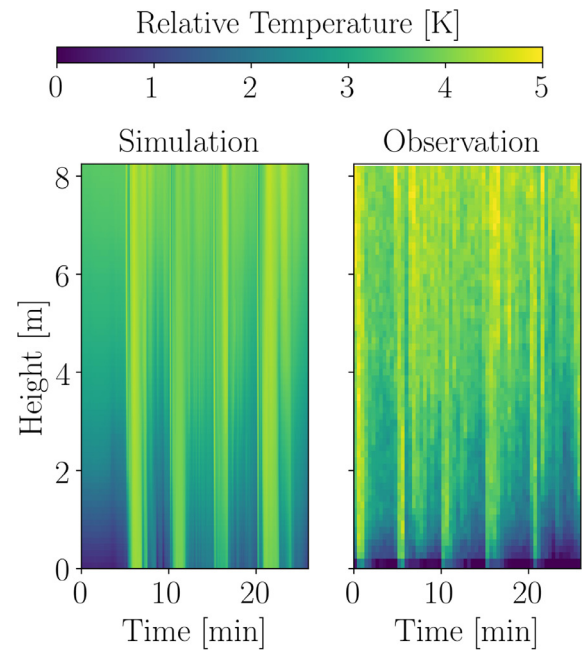
Thus the ‘performance’ of the wind machine can, per simulation run, be summarized to: the influenced area and the area averaged efficiency.

Notice that for runs without a mean wind, the problem is axisymmetric in the horizontal, centred around the wind machine. Consequently, the measure of area can be reduced to a measure of distance (area =  $\pi(\text{distance})^2$ ). The standard deviation of this distance (measured per angle) is used as an estimate for the variability in results between repeated simulations. For Fig. 18 this resulted in an influence distance of  $81 \pm 5$  m and an average efficiency  $0.46 \pm 0.02$ .

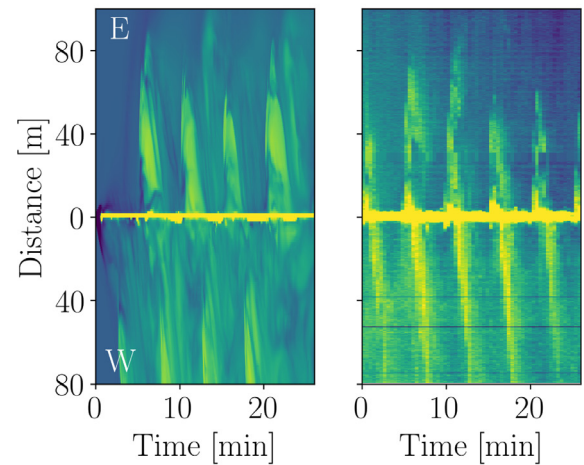
In the next subsections, the analysis will be focussed towards functional relations between parameters and the performance measures. Hereto, only the results for the 2 m height are shown. For completeness, also a true ensemble simulation of 5 times a rerun of the reference case is included in the results.

5.2.1. Rotation time: area strongly dependent

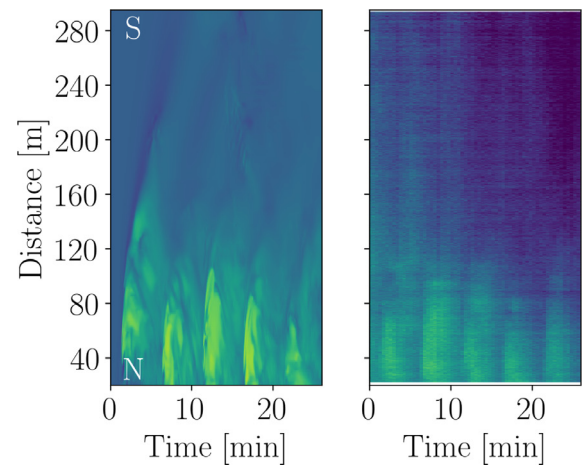
The rotation time,  $\tau$ , was varied between 120 s and 360 s. The total simulation runtime was kept equal to have a constant displaced air volume between runs. Performance measures are shown in Fig. 19. For the longer rotation times ( $\tau > 240$  s) averaging was done over two



(a) Vertical cable, 30 m East of the fan.



(b) Horizontal West-East cable. Note: ambient wind is from the East.



(c) Horizontal North-South cable.

Fig. 16. Time series comparison between the DTS measurements of the simulation (left) and the experiment (right).

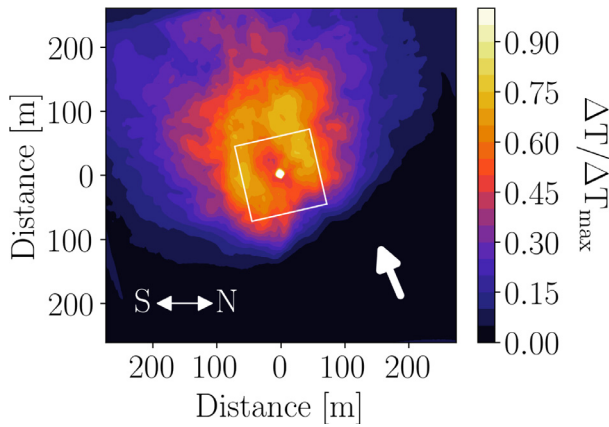


**Fig. 17.** Efficiency at 1 m height with  $\Delta T_{\max} = 1.96$  K. The arrow denotes the wind direction and the white square the area spanned by the sensor grid in the original field experiment, Fig. 13. Note that the white central circle is off-scale, caused by local engine heat.

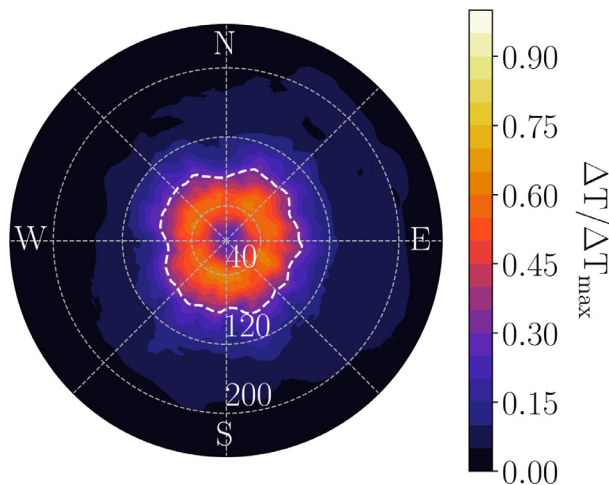


**Fig. 18.** Example showing efficiency in a two dimensional contour plot. The radial distance is in meters. The white dotted line denotes the distance of influence as fitted using the Gaussian model.

rotation cycles only. The influence distance increased linearly with  $\tau$ . This implies that the area,  $A$ , scales with  $\tau^2$ :  $A \propto \tau^2$ . A surprising result, considering that, time averaged, every location had the same ‘jet exposure’. At the same time, the reduction in efficiency with  $\tau$  is only modest. The overall ‘trade-off’ therefore seems to be positive with increasing rotation time. Hence, the aspect of rotation time seems to have a large overall impact. It is therefore recommended to explore this important parameter in future outdoor field studies as well as to optimize fan performance.

**5.2.2. Tilt angle: an optimum?**

The tilt angle,  $\alpha$ , was varied between  $0^\circ$  and  $20^\circ$  as depicted in Fig. 20. The influence distance decreased with increasing angle, which is expected based on the geometry of the problem. Interestingly enough, in the efficiency an ‘optimum’ seems to be reached between  $8^\circ$  and  $16^\circ$ . In visualisations of the flow (not shown) it is observed that for the larger angles (near  $20^\circ$ ) less mixing occurs and that the warm jet deflects upward as a result of an increased buoyancy. Hence, the optimal angle corresponds in that case to near horizontal flow. Presumably, this optimized vertical heat transport is effectively done by shear driven instabilities (Kelvin-Helmholtz like), which typically are generated at jet-flow interfaces.

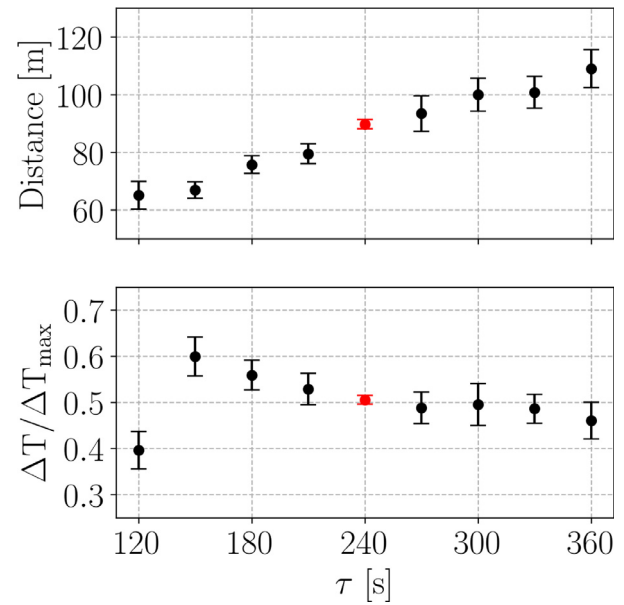


**Fig. 19.** Influence distance and efficiency as a function of rotation time. The error bar is an estimate for the natural variation in the axisymmetric problem, based on 3.75° averages (see text & Fig. 18). The red symbol is based on a five-member ensemble run. (For interpretation of the references to colour in this figure legend, the reader is referred to the web version of this article.)

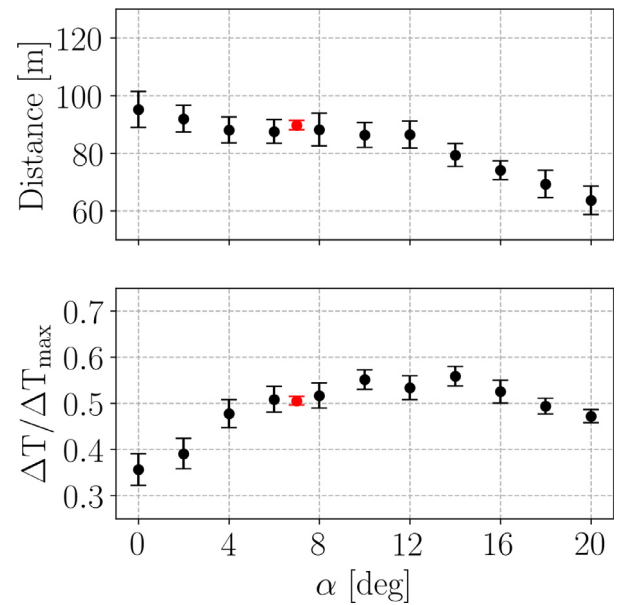


**Fig. 20.** Influence distance and efficiency as a function of tilt angle. The error bar is an estimate for variation between runs. Red denotes the five-member ensemble runs.

**5.2.3. Engine power: linear with heat content**

The engine power,  $P$ , was varied. For clarity reasons, however, results are presented in terms of center jet speed rather than machine power, noting that:  $U_{jet} \propto P^{1/3}$  (see Appendix B.1). The resulting influence distances and efficiencies are shown in Fig. 21. The distance appears linearly proportional to jet speed, hence proportional to  $P^{1/3}$ . The area therefore scales as  $P^{2/3}$  and the efficiency with  $P^{1/3}$ . Finally, the product of area and efficiency is expected to scale with  $P$ . This implies that the heat content in given slab increases more or less linearly with power.

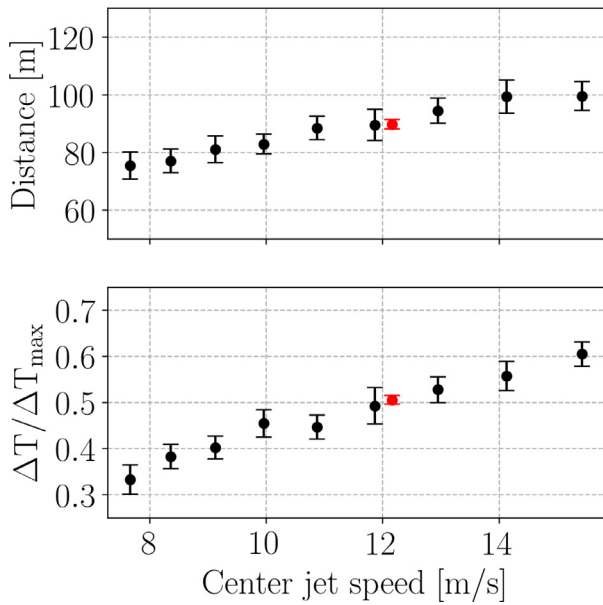


**Fig. 21.** Influence distance and efficiency as a function of center jet speed ( $\propto P^{1/3}$ ). The error bar is an estimate for the variation between runs. Red denotes the five-member ensemble runs.

5.2.4. Ambient wind: a strong asymmetry

The factor,  $U_f$ , was varied, such that the wind speed at hub height,  $U_{10.5}$ , ranged from 0 to 0.74 m/s (Eq. (4)). Since this case is not axisymmetric, the two-dimensional system response is studied. The diagnosed areas of influence are shown in Fig. 22. Interestingly, upwind sensitivity is much less than downwind sensitivity. Even the slightest ambient wind largely reduces the upwind affected area as compared to the downwind area. The average efficiencies, shown in Fig. 23, decreased with increased wind speed. This appears to be caused by a lower maximum efficiency and a larger spatial spreading of the heat (not shown).

5.2.5. Inversion strength: temperature, a passive scalar?

For the inversion strength analysis  $N^2$  was varied between 0.1 and 1.6 K/m, as shown in Fig. 24. No significant relation is seen between the influence distance and the inversion strength. However, the efficiency appears to depend strongly on it. This implies that temperature cannot be regarded as a passive scalar: it reduces temperature enhancement

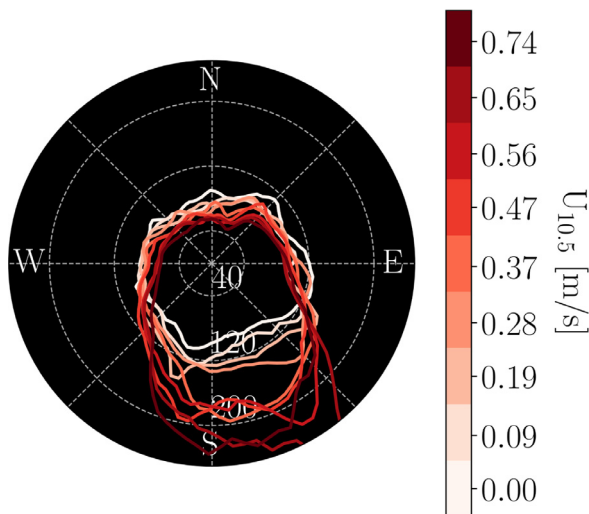


**Fig. 22.** Influence area as a function of fan hub height wind speed,  $U_{10.5}$ . The wind came from the North.

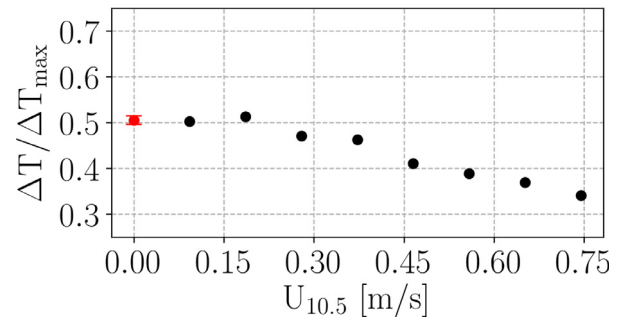


**Fig. 23.** Efficiency as a function of fan hub height wind speed,  $U_{10.5}$ . Red denotes the five-member ensemble runs.

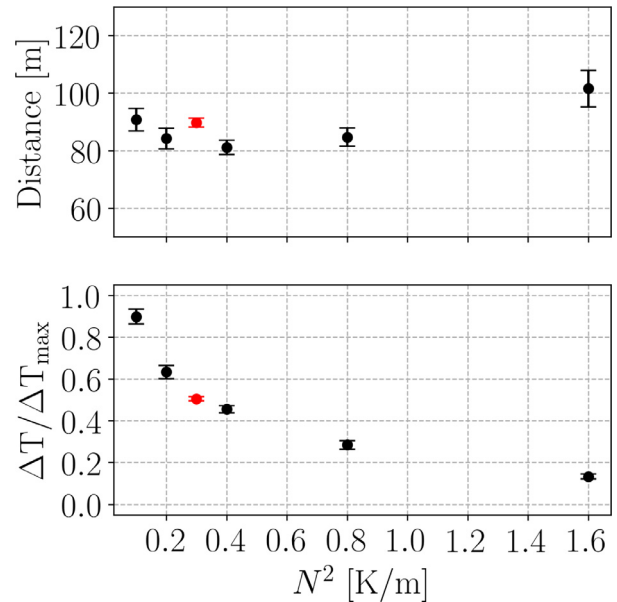


**Fig. 24.** Influence distance and efficiency as a function of  $N^2$ . The error bar is an estimate for the variation between runs. Red denotes the five-member ensemble runs.

even when normalized with the inversion itself! Even more so, with weak inversions, efficiencies tend to 1 so that for weak buoyant forces, temperature indeed seems to behave like a ‘passive scalar’ again. Hence, we conclude that generally buoyant forces do play an important role in suppressing transport in the vertical.

6. Conclusions

In this study we have employed high-resolution measuring techniques to quantify the local temperature response as a result of wind machine operation. As expected, the observations showed that the actual response strongly depends on the distance to the fan and the height above the surface. In agreement with previous studies, the wind machine was able to achieve rotation-averaged temperature increases up to 50% of the inversion strength ( $\approx 3$  K) in an area of 3–5 ha. Furthermore, it was observed that low wind speeds ( $< 1$  m/s) can cause strong upwind-downwind asymmetries in jet velocity and protected area. Downwind the jet reached further and the affected area was larger as compared to upwind. Finally, it was observed that the engine heat and radiation contributes significantly to the local temperature increase. This aspect was given less attention in the past, but could be detected unambiguously with the DTS observations.

In addition to the field experiment, the impact of wind machine operation on the local temperature was studied using turbulence resolving Large Eddy Simulations. It was shown that the spatial

temperature response in the simulations was very similar to observed responses. A strong asymmetry in the perturbed wind field was found in the simulations in accordance with the outcome of the field experiment. From this it is concluded that the simulations provide a reasonably realistic ‘surrogate’ for the field experiment in order to do a well-controlled sensitivity study. This to study wind machine performance in response to different forcing parameters.

Performance was expressed in terms of the size of the affected area and the achieved temperature enhancement (relative to the background inversion). In essence, the eventual inversion strength is a result of gradient eroding and gradient restoring processes. While, obviously, mixing with warm air from aloft erodes the inversion, it is restored by advection of ambient air, buoyant forces and lateral mixing with cold air within the canopy layer.

Interestingly, it was found that wind machine performance strongly depends on the axial rotation time of the machine. Where temperature enhancement remained relatively constant over different rotation rates (ranging from 3 to 6 min), the affected area strongly increased for slower rotations! Apparently, one persistent long mixing ‘burst’ due to slow jet passage, is more beneficial than several short ones. This finding could have important practical consequences and needs to be explored in more depth in the future as to find optimal rotation rates. Note, that a caveat of the present study is that the impact of rotation was studied only for cases without background flow. As such, further exploration is needed in the future to draw definite conclusions.

Investigation of the effect on performance of different tilt angles showed that, in our model, temperature enhancement was maximized between an 8° and 16° tilt angle. Presumably those small angles are very effective in generating strong shear layers which in turn generate Kelvin-Helmholtz type of instabilities. This process increases vertical transport and mixing of heat. Finally, analysis of the sensitivity to the ambient wind speed showed that a strong upwind-downwind asymmetry exists with respect to the affected area. This is in agreement with the findings of our field study.

We believe that future experiments would benefit from similar

## Appendix A. Experimental background

### A1. Influence of the oosterschelde

To study the influence of the Oosterschelde, a high-resolution forecast of the study area was done using the GRASP LES model on a GPU machine by weather research company Whiffle ([www.whiffle.nl](http://www.whiffle.nl), Schalkwijk et al., 2015). The LES was externally forced by data from the numerical weather prediction model ECMWF for January 20, 2019. Cases with a 5 by 5 km horizontal and 2.5 km vertical domain were run, one with high and one with low tide. The average wind speed slices at 3 m height during wind machine operation are shown in Fig. 25 for both cases.

Significant differences are seen both in wind speed and direction. The presence of relatively warm and rough water decreases the stability and thus favors momentum transport towards the surface. This implies that radiation frost events are less likely to occur during high tide than during low tide.

### A2. Soil cover

### A3. Data fitting parameters

The full range of fitted parameters to the experimental data (Table 1) are shown in Table 2. Note that negative covariances can result in lower fitting uncertainties in measures consisting of multiple parameters (i.e. Distance and Max Efficiency).

## Appendix B. Simulation background

### B1. Wind machine implementation

The implementation is based on a momentum forcing. An amount of work per time is done on the flow with a certain power,  $P$ . Using the work-energy theorem, which states that the work done by all acting forces on a particle is equal the change in kinetic energy, this can be expressed as  $\Delta E_{\text{kin}} = P\Delta t$ . This directly implies that,

studies. In particular, experiments in which the size of the horizontal sensor grid is extended and wind data with higher spatial resolution is obtained. Furthermore, multiple vertical profiles could be put in every cardinal direction of the wind machine and measurement distance could be extended in the downwind direction. These unshielded temperature sensors should be augmented with shielded variants to ‘calibrate’ the sensors at regular intervals. This will allow for a better understanding of the height varying temperature enhancement, and the asymmetries caused by the ambient wind. In addition, data should be gathered on a multitude of nights such that a composite study can be made similar to van der Linden et al. (2017). From a model perspective, our results can be improved by implementing (parametrizations of) tree geometries and by using a more realistic description of the prescribed wind and temperature profiles (i.e. non-linear shapes). In view of the authors, it would be both interesting and relevant to extend the philosophy of the present study to other frost mitigation measures at the field scale, so that in the future optimal strategies can be distilled in order to fight frost damage in an effective way.

## Declaration of Competing Interest

None.

## Acknowledgments

We are grateful to Martijn Vogelaar of Vogelaar Fruitcultures for providing the experimental site and for sharing his impressive practical experience. We also thank Freek van de Wiel, Cynthia Maan, Charlotte Ziedorn, Mariska Koning and Rene Reudink for their roles in the preparation and deployment of the experimental setup. Maarten Kruis, Jonathan Izett and Steven van der Linden are thanked in particular for their contributions to the former and subsequent discussions. Finally, Erwin de Beus is thanked for facilitating and maintaining computational infrastructure used in this study.

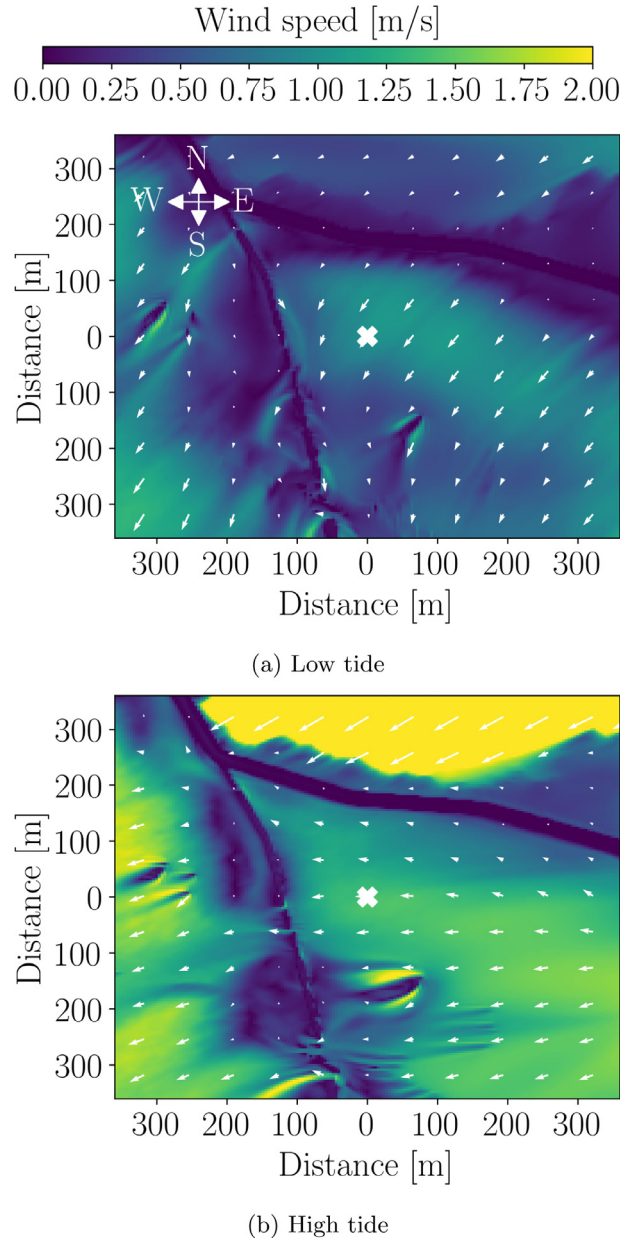


**Fig. 25.** Average 3 m wind speed during the experiment using a high-resolution forecast, comparing low and high tide. The cross denotes the position of the fan and the arrows indicate the magnitude and direction of the near surface wind vectors.

$$\vec{v}_{t+\Delta t}^2 - \vec{v}_t^2 = \frac{2P\Delta t}{m} \hat{n}^2 \quad (7)$$

which in turn implies for every spatial dimension,

$$v_{i,t+\Delta t}^2 - v_{i,t}^2 = \frac{2P\Delta t}{m} n_i^2 \quad (8)$$

with  $m$  the air mass (or rather the density). From these equations the direction of  $\hat{n}$  is not yet defined and  $|\hat{n}| = 1$ . When it is assumed that the force applied to the flow is normal to the plane in which the fan blades rotate then  $\hat{n}$  is the normal vector of this plane. Rearranging Eq. (8) and taking the square root results in,

$$\vec{v}_{i,t+\Delta t} = \sqrt{\vec{v}_{i,t}^2 + \frac{2P\Delta t}{m} \hat{n}_i^2} \quad (9)$$

For the numerical implementation see: <http://basilisk.fr/sandbox/vheusinkveld/fan.c>.

From Eq. (9) it is not clear to what velocity an air parcel subject to the forcing will be accelerated to. We move to a continuous calculation such that we can use calculus. For this, we assume that the air parcel enters the forcing at  $t_{start}$  and leaves at  $t_{end}$ , moving a distance  $l$  in the process:

$$l = \int_{t_{start}}^{t_{end}} v(t) dt \quad (10)$$



Fig. 26. Alternating soil cover of litter under the trees and grass between the rows. The 1 m and 0 m West-East cables are also visible.

Table 2

Fitting parameters to the experimental data. Fitting uncertainties smaller than the least significant digit are not shown.

Section	a	b [m]	c [m]	d
South 1 m	0.5	40.0 ± 0.5	43.9 ± 0.4	0.0
West 1 m	0.53 ± 0.89	23.5 ± 3.0	81.2 ± 78.3	± 0.9
East 1 m	0.37 ± 0.02	29.6 ± 1.1	38.2 ± 2.0	± 0.02
West 0 m	0.53 ± 0.4	14.3 ± 6.7	62.3 ± 35.0	± 0.4
East 0 m	0.44 ± 0.01	27.0 ± 1.0	24.4 ± 1.1	± 0.01

Assuming a zero entrance velocity at  $t_{start} = 0$ ,  $v$  is given as:

$$E_{kin} = P\Delta t = 0.5mv^2$$

$$v(t) = \sqrt{2Pt/m} \quad (11)$$

$P$ ,  $l$  and  $m$  are chosen properties in the simulation. Hence Eq. (10) can be solved for  $t_{end}$  by substituting the expression for  $v(t)$ . The corresponding exit velocity is given as:

$$v_{end} = \left(\frac{3Pl}{m}\right)^{1/3} \quad (12)$$

## References

- Bates, E.M., Lombard, P.B., et al., 1978. Evaluation of Temperature Inversions and Wind Machine on Frost Protection in Southern Oregon. Technical Report. Oregon State University. Agricultural Experiment Station.
- Bell, J.B., Colella, P., Glaz, H.M., 1989. A second-order projection method for the incompressible Navier-Stokes equations. *J. Comput. Phys.* 85 (2), 257–283. [https://doi.org/10.1016/0021-9991\(89\)90151-4](https://doi.org/10.1016/0021-9991(89)90151-4).
- Bense, V.F., Read, T., Verhoef, A., 2016. Using distributed temperature sensing to monitor field scale dynamics of ground surface temperature and related substrate heat flux. *Agric. For. Meteorol.* 220, 207–215. <https://doi.org/10.1016/j.agrformet.2016.01.138>.
- Berz, G., 1992. Losses in the range of US \$50 billion and 50 000 people killed: Munich Re's list of major natural disasters in 1990. *Nat. Hazards* 5 (1), 95–102.
- Bey-Marshall, V., Herrera, J., Santibez, F., Fichet, T., 2019. Microclimate modification under the effect of stationary and portable wind machines. *Agric. For. Meteorol.* 269–270, 351–363. <https://doi.org/10.1016/j.agrformet.2019.01.042>.
- Boing, S., Jonker, H. J. J., van de Wiel, B. J. H., Moene, A. F., 2010. Intermittent turbulence in stratified flow over a canopy. Extended Abstracts, 19th Symp. on Boundary Layers and Turbulence, Keystone, CO, Amer. Meteor. Soc., 7.2. Available online at <http://ams.confex.com/ams/pdfpapers/172716.pdf>.
- Brandt, A., 1977. Multi-level adaptive solutions to boundary-value problems. *Math. Comput.* 31 (138), 333–390.
- Brooks, F., Rhoades, D., Leonard, A., et al., 1954. Wind machine tests in citrus: frost protection studies in 1954 confirmed earlier findings next to be investigated in deciduous trees. *Calif. Agric.* 8 (8), 8–10.
- Castillo-Castellanos, A.A., 2017. Turbulent Convection in Rayleigh-Bénard Cells with Modified Boundary Conditions. Université Pierre et Marie Curie Ph.D. thesis.
- des Tombe, B., Schilperoort, B., 2019. dtscalibration/python-dts-calibration: v0.6.4. 10.5281/zenodo.2633840.
- Evans, R.G., 1999. Frost Protection in Orchards and Vineyards. Washington State Univ. Coop. Ext. Pullman.
- Finnigan, J.J., Shaw, R.H., Patton, E.G., 2009. Turbulence structure above a vegetation canopy. *J. Fluid Mech.* 637, 387–424. <https://doi.org/10.1017/S0022112009990589>.
- Google Maps. XYZ tile server. Krabbendijke, 51°25'44.7"N, 4°, 8'8.5"E. Retrieved on: 2019-01-18 <http://mt0.google.com/vt/lyrs=s&hl=en&x=x&y=y&z=z>.
- Izett, J.G., Schilperoort, B., Coenders-Gerrits, M., Baas, P., Bosveld, F.C., van de Wiel, B.J.H., 2019. Missed fog? Boundary-Layer Meteorol. 173 (2), 289–309. <https://doi.org/10.1007/s10546-019-00462-3>.
- Kalma, J.D., Laughlin, G.P., Caprio, J.M., Hamer, P.J.C., 1992. The Bioclimatology of Frost: Its Occurrence, Impact and Protection. *Advances in Bioclimatology*, vol. 2 Springer.
- Popinet, S., 2009. An accurate adaptive solver for surface-tension-driven interfacial flows. *J. Comput. Phys.* 228 (16), 5838–5866. <https://doi.org/10.1016/j.jcp.2009.04.042>.
- Popinet, S., 2015. A quadtree-adaptive multigrid solver for the Serre–Green–Naghdi equations. *J. Comput. Phys.* 302, 336–358. <https://doi.org/10.1016/j.jcp.2015.09.009>.
- Ribeiro, A.C., Melo-Abreu, J.P.D., Snyder, R.L., 2006. Apple orchard frost protection with wind machine operation. *Agric. For. Meteorol.* 141 (2–4), 71–81. <https://doi.org/10.1016/j.agrformet.2006.08.019>.
- Schalkwijk, J., Jonker, H.J.J., Siebesma, A.P., Van Meijgaard, E., 2015. Weather forecasting using GPU-based large-eddy simulations. *Bull. Am. Meteorol. Soc.* 96 (5), 715–723.
- Scharringa, M., 1962. Nachtvorst. 's-Gravenhage: Staatsdrukkerij.
- Schilperoort, B., Coenders-Gerrits, M., Luxemburg, W., Rodríguez, C.J., Vaca, C.C., Savenije, H., 2018. Technical note: using distributed temperature sensing for Bowen ratio evaporation measurements. *Hydrol. Earth Syst. Sci.* 22 (1), 819–830. <https://doi.org/10.5194/hess-22-819-2018>.
- Selker, J.S., Thévenaz, L., Huwald, H., Mallet, A., Luxemburg, W., van de Giesen, N., Stejskal, M., Zeman, J., Westhoff, M., Parlange, M.B., 2006. Distributed fiber-optic

- temperature sensing for hydrologic systems. *Water Resour. Res.* 42 (12). <https://doi.org/10.1029/2006wr005326>.
- Smolen, J. J., van der Spek, A., 2003. *Distributed Temperature Sensing: A DTS Primer for Oil & Gas Production*. Shell.
- Snyder, R.L., de Melo-Abreu, J.P., 2005. *Frost Protection: Fundamentals, Practice, and Economics*. vol. 1 Food and Agriculture Organization of the United Nations.
- Thomas, C.K., Kennedy, A.M., Selker, J.S., Moretti, A., Schroth, M.H., Smoot, A.R., Tuffillaro, N.B., Zeeman, M.J., 2011. High-resolution fibre-optic temperature sensing: a new tool to study the two-dimensional structure of atmospheric surface-layer flow. *Boundary-Layer Meteorol.* 142 (2), 177–192. <https://doi.org/10.1007/s10546-011-9672-7>.
- van de Wiel, B.J.H., Vignon, E., Baas, P., van Hooijdonk, I.G.S., van der Linden, S.J.A., van Hooft, J.A., Bosveld, F.C., de Roode, S.R., Moene, A.F., Genthon, C., 2017. Regime transitions in near-surface temperature inversions: a conceptual model. *J. Atmos. Sci.* 74 (4), 1057–1073. <https://doi.org/10.1175/jas-d-16-0180.1>.
- van der Linden, S.J.A., Baas, P., van Hooft, J.A., van Hooijdonk, I.G.S., Bosveld, F.C., van de Wiel, B.J.H., 2017. Local characteristics of the nocturnal boundary layer in response to external pressure forcing. *J. Appl. Meteorol. Climatol.* 56 (11), 3035–3047. <https://doi.org/10.1175/jamc-d-17-0011.1>.
- van Hooft, J.A., Popinet, S., van de Wiel, B.J.H., 2018. Adaptive cartesian meshes for atmospheric single-column models, a study using basilisk 18-02-16. *Geosci. Model Dev. Discuss.* 1–14. <https://doi.org/10.5194/gmd-2018-21>.
- van Hooft, J.A., Popinet, S., van Heerwaarden, C.C., van der Linden, S.J.A., de Roode, S.R., van de Wiel, B.J.H., 2018. Towards adaptive grids for atmospheric boundary-layer simulations. *Boundary-Layer Meteorol.* 167 (3), 421–443. <https://doi.org/10.1007/s10546-018-0335-9>.
- van Hooft, J.A., Baas, P., van Tiggelen, M., Anson, C., van de Wiel, B.J.H., 2019. An idealized description for the diurnal cycle of the dry atmospheric boundary layer. *J. Atmos. Sci.* 76, 3717–3736. <https://doi.org/10.1175/JAS-D-19-0023.1>.
- Vreman, A.W., 2004. *An eddy-viscosity subgrid-scale model for turbulent shear flow: algebraic theory and applications*. *Phys. Fluids* 16 (10), 3670–3681.
- White, G.F., Haas, J.E., 1975. *Assessment of Research on Natural Hazards*. Massachusetts Institute of Technology Press.
- Wyngaard, J.C., 2010. *Turbulence in the Atmosphere*. Cambridge University Press.
- Zeeman, M.J., Selker, J.S., Thomas, C.K., 2014. Near-surface motion in the nocturnal, stable boundary layer observed with fibre-optic distributed temperature sensing. *Boundary-Layer Meteorol.* 154 (2), 189–205. <https://doi.org/10.1007/s10546-014-9972-9>.